Available online at www.sciencedirect.com
SCIENCE DIRECT®
Journal of Computational Physics 195 (2004) 387–412
JOURNAL OF COMPUTATIONAL PHYSICS
www.elsevier.com/locate/jcp

A Karhunen–Loève least-squares technique for optimization of geometry of a blunt body in supersonic flow ☆

Gregory P. Brooks [a,1], Joseph M. Powers [b,*,2]

[a] Air Force Research Laboratory, Wright-Patterson AFB, Ohio 45433, USA
[b] Department of Aerospace and Mechanical Engineering, University of Notre Dame, Notre Dame, IN 46556-5637, USA

Received 21 February 2003; received in revised form 25 August 2003; accepted 26 August 2003

Abstract

A novel Karhunen–Loève (KL) least-squares model for the supersonic flow of an inviscid, calorically perfect ideal gas about an axisymmetric blunt body employing shock-fitting is developed; the KL least-squares model is used to accurately select an optimal configuration which minimizes drag. Accuracy and efficiency of the KL method is compared to a pseudospectral method employing global Lagrange interpolating polynomials. KL modes are derived from pseudospectral solutions at Mach 3.5 from a uniform sampling of the design space and subsequently employed as the trial functions for a least-squares method of weighted residuals. Results are presented showing the high accuracy of the method with less than 10 KL modes. Close agreement is found between the optimal geometry found using the KL model to that found from the pseudospectral solver. Not including the cost of sampling the design space and building the KL model, the KL least-squares method requires less than half the central processing unit time as the pseudospectral method to achieve the same level of accuracy. A decrease in computational cost of several orders of magnitude as reported in the literature when comparing the KL method against discrete solvers is shown not to hold for the current problem. The efficiency is lost because the nature of the nonlinearity renders a priori evaluation of certain necessary integrals impossible, requiring as a consequence many costly reevaluations of the integrals.

Keywords: Karhunen–Loève; Least-squares; Shock-fitting; Optimal design; Euler equations; Pseudospectral method

1. Introduction

Computer-assisted multi-disciplinary design and optimization in the aeronautical engineering community is a promising area of current research. The optimization of air vehicles has often relied on low fidelity

☆ This study has received primary support from the United States Air Force Palace Knight Program and additional support from Los Alamos National Laboratory.
* Corresponding author. Tel.: +1-574-631-5978; fax: +1-574-631-8341.
E-mail addresses: Gregory.Brooks@wpafb.af.mil (G.P. Brooks), powers@nd.edu (J.M. Powers).
[1] Research Aerospace Engineer.
[2] Associate Professor.

0021-9991/$ - see front matter
doi:10.1016/j.jcp.2003.08.030

aerodynamic models due to the need for rapid evaluation of aerodynamic design variables such as lift, drag, or heat transfer. Unfortunately, the use of low fidelity models can lead to unacceptable uncertainties in the final optimal design, especially where design safety margins are tight [1]. In addition, low fidelity models often do not provide the complete flow field information such as pressure, temperature, and velocity distributions, acoustic signature, shock wave location, which the designer may require. For these reasons, high fidelity models such as the Euler or Navier–Stokes equations are often required. For most problems, these model equations can be solved only after discretization.

Brooks [2] and Brooks and Powers [3,4] describe an adaptation of the work of Kopriva et al. [5] for a shock-fitted pseudospectral method for the numerical approximation to the steady-state inviscid supersonic flow around a blunt body geometry. The unsteady Euler equations and associated boundary conditions are cast in the form of a system of ordinary differential equations (ODEs) and integrated to a long time steady-state solution. Grid convergence of the error in the pseudospectral approximation measured against a fine grid approximation exhibits high accuracy and a spectral convergence rate. The shock is fitted since approximation of discontinuous solutions with high-order polynomials exhibit the Gibbs phenomenon in the form of global oscillations in the solution [6]. These oscillations can cause the numerical scheme to become unstable and attempts to remove the oscillations by spectral filtering or by addition of artificial viscosity significantly reduces the accuracy of the numerical method. The more common alternative of shock capturing, while generally stable and non-oscillatory, yields only first-order accuracy.

A major difficulty in employing discrete solvers in a multi-disciplinary design process is the large central processing unit (CPU) requirements of these codes. It is not uncommon for discrete solutions to three-dimensional flows around complex aircraft configurations to require on the order of 10 or more hours of CPU time per steady-state solution [1], and these solutions are likely not fully resolved. Complete resolution of complex flow structures could require considerably more CPU time. A design incorporating multiple disciplines, e.g., aerodynamics, structures, controls, may easily have hundreds or even thousands of design variables. While interdisciplinary coordination schemes using varying fidelity models [7] help to alleviate the CPU cost associated with interdisciplinary dependence, the aerodynamics discipline alone could still involve hundreds or more design variables. For this reason, current gradient-based numerical optimizers can be prohibitively expensive when used directly with discrete solvers of high fidelity models, and approximation becomes necessary.

One popular approximation technique for the design of complex, multi-variable problems is the response surface approximation [8]. Response surfaces typically approximate quantities such as the lift and drag of the vehicle as a function of the design variables, e.g., geometric parameters, in terms of simple functional forms. An advantage of the response surface method is that both objective function and gradient evaluation are rapid, on the order of 1 s or less. Furthermore, polynomial approximation of the objective function ensures that the gradients are continuous. This increases the efficiency of the numerical optimizer in the sense that fewer iterations may be needed to reach an optimum. Two disadvantages of the response surface method are a potential lack of accuracy in capturing the system response by a simple function and also the absence of detailed information about the flow field. Flow field information may be needed for design of a thermal protection system, for coupling with a structural code in static and aeroelastic design, for inverse vehicle design in sonic boom mitigation, acoustic or radar signature reduction, or for shock wave placement for efficient supersonic/hypersonic propulsion.

A recently developed method which does yield detailed flow field information by solution of the governing equations such as the Euler or Navier–Stokes equations is the adjoint method [9–11] adopted from control theory [12]. This method is computationally efficient for gradient-based optimizers since objective function gradients with respect to an arbitrary number of design variables can be computed exactly by solving the governing equations plus an adjoint equation. Since the adjoint equation is of similar complexity as the governing equations, each iteration of the optimizer regardless of the number of design variables is equivalent in computational cost to two flow field solutions. The fact that the computational

cost of the adjoint method does not increase with the number of design variables is a significant advantage over the response surface method whose computational cost increases with increasing number of design variables. Although still in development, the adjoint method appears to be promising as an accurate and efficient means of multi-disciplinary, multi-variable optimal design. Nevertheless, the adjoint method has the disadvantage of requiring that a unique adjoint equation be derived and solved for each new design objective function that may be formulated.

Another approximation technique is the Karhunen–Loève (KL) method. This technique is a method of weighted residuals where the trial functions are eigenfunctions of the averaged auto-correlation of previous numerical flow-field solutions. It can be shown that the KL decomposition yields an optimal set of orthonormal basis functions in the sense that the fewest number of functions of all possible bases are required for a given level of accuracy in reconstructing the original set of data. Employing the KL modes as the trial functions of a Galerkin [13], orthogonal collocation [14], or least-squares [15] method of weighted residuals reduced dimension models have been developed which yield accurate solutions to partial differential equations for a computational cost several orders of magnitude lower than discrete solvers for the same level of accuracy. Park and Jung [16], for example, report CPU times of 7.5 h and 11 min, respectively, for arriving at an optimal control law for magnetic suppression of natural convection using a pseudospectral and a KL Galerkin method. In the case of Park and Jung [16], the nonlinearity of their problem was quadratic, so that it was possible to evaluate the spatial integrals in the KL Galerkin model only once at the time when the model was built. This led to a significant reduction in the degrees of freedom of the KL Galerkin model over the pseudospectral solver and consequent reduction in computational cost.

Advantages of the KL method over response surfaces are generation of detailed flow field information and potential increase in accuracy. The KL method also has advantages over the adjoint method in that the KL model is independent of the design problem formulation. This flexibility in specifying the design problem is an important attribute for an optimal design code [17].

We next review some applications of the KL theory in control, optimization, and modelling of thermofluid systems. The KL decomposition has been used in conjunction with the Galerkin method of weighted residuals to develop approximate models of turbulent fluid mechanical phenomena, e.g., Aubry et al. [18], and Sirovich and Park [19,20]. The first use of the KL method for a control application was by Chen and Chang [21], where it was used to control spatiotemporal patterns on a catalytic wafer using experimentally determined KL modes. Independently, Park and Cho [22] developed a KL Galerkin model of a nonlinear heat equation for control or parameter estimation [23–28]. The KL Galerkin method has also been used to approximate Navier–Stokes solutions for flow control [29–31] applications. In order to avoid the difficulty of employing the Galerkin method for nonlinear problems, Theodoropulou et al. [14] successfully implemented an orthogonal collocation method with numerical KL modes for the optimization of rapid thermal chemical vapor deposition systems in one dimension. LeGresley and Alonso [15] used a KL least-squares model of the Euler equations in a finite volume formulation to optimize the pressure distribution around an airfoil in subsonic flow and more recently extended the method via domain decomposition to include the high subsonic region with mild shocks [32]. A KL model for the high speed flow over a two-dimensional blunt body using a subspace projection method and domain decomposition was developed by Lucia [33]. In the domain decomposition method, the region around the shock is isolated and a KL model is developed for the smooth region of the flow, while the region containing the shock can be solved using the full system model.

The first step in generating a KL model is to develop a set of numerical solutions to the governing equations for a range of design variables or in this case, a single design variable. In general, high accuracy solutions are desirable so that more high order, low amplitude KL modes can be accurately resolved from the set of numerical solutions. Any consistent and stable numerical method could be chosen to generate high accuracy solutions; the pseudospectral method described by Brooks and his colleague [2,4] is the one chosen for this study. The pseudospectral method has the advantage of an exponential grid convergence rate for sufficiently smooth solutions; consequently, relative to finite difference or finite element methods

with polynomial convergence rates, pseudospectral methods can generally achieve the same absolute error with a smaller computational cost, or for the same computational effort, pseudospectral methods generate a more accurate solution than finite difference or finite element methods. In addition, since the solution is known in terms of Lagrange interpolating polynomials, the KL modes can also be expressed in terms of Lagrange polynomials and integration of the KL modes necessary for the least-squares method can be performed exactly by means of Gaussian quadrature, thus maintaining the high accuracy of the method.

The second step in the development of the KL model is to perform a KL decomposition on the characteristic solution set generated by the flow solver. The KL decomposition, also called proper orthogonal decomposition (POD), appears to have been developed independently in the 1940s by several researchers including Karhunen [34] and Loève [35]. Lumley [36] proposed the KL decomposition as a rational procedure for the extraction of coherent structures in a turbulent flow field. The KL decomposition is also closely related to the singular value decomposition and principal component analysis used in data compression and image processing [37]. As originally introduced by Lumley, the KL decomposition was impractical for more than one spatial dimension. It was not until Sirovich [38] introduced the method of snapshots that the KL decomposition became practical for highly resolved, three-dimensional flows.

The final step in the development of the KL model is to approximate the governing equations and boundary conditions in a series expansion of the KL modes and solve for the coefficients in the expansion via a least-squares, Galerkin, or collocation method of weighted residuals. For the current paper, a KL least-squares model will be developed.

In the remainder of this paper, the three main steps just described for developing a KL least-squares model are presented for a model partial differential equation. Following this, the blunt body problem is posed. Since the error in the blunt body pseudospectral solver was found to decrease uniformly over a range of Mach numbers, which is not the case when the geometry is varied, a KL model is built by varying the Mach number. Ten pseudospectral solutions, also referred to as snapshots, are generated for 10 different values of Mach number, and the corresponding 10 KL modes are presented. The KL least-squares model of the blunt body problem is subsequently presented along with error convergence plots with respect to the number of KL modes used in the model. The error in the KL model is measured against a highly resolved solution from the pseudospectral solver. A single-variable optimal design problem is then solved using both the KL least-squares model and the pseudospectral solver. Ten pseudospectral solutions are generated for 10 different values of a single geometric design variable, and the corresponding 10 KL modes are presented. Error convergence plots with respect to the number of KL modes are also presented for this model. The accuracy and efficiency of the KL model is compared to that of the pseudospectral solver for the single-variable optimal design problem. Comparison of the operation count for the KL least-squares model versus the pseudospectral method are also presented.

2. KL design optimization strategy

2.1. Step 1: Flow solver

The first step in developing a KL model for use in optimization is to generate a set of K characteristic solutions which span the design space of interest in the problem. In the current study, the design space is parameterized by a single geometric variable, b. The method can be extended to multi-variable optimization problems. Let us consider the following system of time-dependent partial differential equations, boundary conditions, and initial conditions in two space dimensions, ξ and η, defined over the domain

$$\Omega : \{\xi \in [0,1],\ \eta \in [0,1]\}, \tag{1}$$

and bounded by S,

$$\frac{\partial \mathbf{y}}{\partial \tau} + \mathbf{f}\left(\mathbf{y}, \frac{\partial \mathbf{y}}{\partial \xi}, \frac{\partial \mathbf{y}}{\partial \eta}\right) = \mathbf{0}, \tag{2}$$

$$\mathbf{g}\left(\mathbf{y}, \frac{\partial \mathbf{y}}{\partial \xi}, \frac{\partial \mathbf{y}}{\partial \eta}\right) = \mathbf{0}, \tag{3}$$

along with the initial conditions,

$$\mathbf{y}(\xi, \eta, 0) = \mathbf{y}_0(\xi, \eta), \tag{4}$$

where for the current problem, $\mathbf{y}(\xi, \eta, \tau) : \mathbb{R}^3 \to \mathbb{R}^{10}$, $\mathbf{f} : \mathbb{R}^3 \to \mathbb{R}^{10}$, and $\mathbf{g} : \mathbb{R}^3 \to \mathbb{R}^{11}$. The function $\mathbf{y}(\xi, \eta, \tau; b)$ consists of six terms, $y^q(\xi, \eta, \tau; b)$, $q = 1, \ldots, 6$, defined over Ω and four terms, $y^q(\xi, \eta, \tau; b)$, $q = 7, \ldots, 10$, defined over S. All of the algebraic constraints, Eq. (3), are boundary conditions and thus apply only on S. Although Eq. (2) is time-dependent, for the optimal design problem only steady-state solutions for various values of b are considered. Solving the time-dependent equation to a relaxed steady state is a convenient numerical solution technique and computationally easier than directly solving the formally steady problem, although computationally less efficient.

The system of equations in Eqs. (2) and (3) along with initial conditions, Eq. (4) are solved for K distinct values of the geometric variable, b_k, $k = 1, \ldots, K$, at steady state. We make the following definition:

$$\mathbf{X}(\boldsymbol{\xi}) = X_k^q(\xi, \eta) = y^q(\xi, \eta, \tau \to \infty; b_k), \quad q = 1, \ldots, 6, \;\; k = 1, \ldots, K \tag{5}$$

and construct the following $K \times 6$ matrix of functions $\mathbf{X}(\boldsymbol{\xi})$:

$$\mathbf{X}(\boldsymbol{\xi}) = \begin{bmatrix} X_1^1(\boldsymbol{\xi}) & \cdots & X_K^1(\boldsymbol{\xi}) \\ \vdots & \ddots & \\ X_1^6(\boldsymbol{\xi}) & & X_K^6(\boldsymbol{\xi}) \end{bmatrix}. \tag{6}$$

The function $\mathbf{X}(\boldsymbol{\xi})$ contains a solution for a particular geometry b_k in each of its columns; the rows of $\mathbf{X}(\boldsymbol{\xi})$ are composed of a particular independent variable for the span of the geometries. Here we take $\boldsymbol{\xi} = \xi, \eta$.

2.2. Step 2: Karhunen–Loève Theory

The second step in the development of the KL model is to perform a separate KL decomposition on each row of $\mathbf{X}(\boldsymbol{\xi})$. Since there are six rows corresponding to the four dependent flow field variables plus the two physical coordinates, the KL decomposition will be performed six times. Brooks [2] gives details of a standard analysis showing that the eigenfunctions, $\varphi_k^q(\boldsymbol{\xi})$, $k = 1, \ldots, K$, of the kernel $\mathbf{R}^q(\boldsymbol{\xi}, \boldsymbol{\xi}') = \frac{1}{K} \sum_{k=1}^{K} X_k^q(\boldsymbol{\xi}) X_k^q(\boldsymbol{\xi}')$, are orthonormal and form on average the most efficient linear basis, in a least-squares error sense, for constructing a truncated series approximation to any of the $X_k^q(\boldsymbol{\xi})$, $k = 1, \ldots, K$, where $q = 1, \ldots, 6$, denote the dependent variables of the problem.

2.3. Step 3: Least-squares method of weighted residuals

The final step in developing a KL model of a differential equation is to expand the $y^q(\xi, \eta, \tau \to \infty; b)$, $q = 1, \ldots, 6$, defined over Ω in terms of the KL modes, $\varphi_k^q(\xi, \eta)$, $q = 1, \ldots, 6$, $k = 1, \ldots, K$, from step 2. Let us consider a steady-state form of Eq. (2),

$$\widehat{\mathbf{f}}\left(\widehat{\mathbf{y}}, \frac{\partial \widehat{\mathbf{y}}}{\partial \xi}, \frac{\partial \widehat{\mathbf{y}}}{\partial \eta}\right) = \mathbf{0}, \tag{7}$$

$$\widehat{\mathbf{g}}\left(\widehat{\mathbf{y}}, \frac{\partial \widehat{\mathbf{y}}}{\partial \xi}, \frac{\partial \widehat{\mathbf{y}}}{\partial \eta}\right) = \mathbf{0}, \tag{8}$$

where $\widehat{\mathbf{y}}(\xi,\eta)$ is of dimension six, corresponding to $y^q(\xi,\eta,\tau\to\infty;b)$, $q=1,\ldots,6$, $\widehat{\mathbf{f}}$ is of dimension four also defined over Ω, and $\widehat{\mathbf{g}}$ is of dimension eight and defined over S. For the current supersonic blunt body problem, the six terms in $\widehat{\mathbf{y}}(\xi,\eta)$ are the density, pressure, two velocity components, and two physical grid coordinates, the four components of $\widehat{\mathbf{f}}$ are the steady-state form of the Euler equations and the eight components of $\widehat{\mathbf{g}}$ are the appropriate nonlinear boundary conditions. The dimension of $\widehat{\mathbf{g}}$ is reduced from the dimension of $\mathbf{g}$ because linear boundary conditions are not included in $\widehat{\mathbf{g}}$ since they are automatically satisfied by the KL approximation as will be elaborated in a subsequent section. The reduction in the dimensions for $\widehat{\mathbf{y}}$ and $\widehat{\mathbf{f}}$ compared to $\mathbf{y}$ and $\mathbf{f}$, respectively, is a result of eliminating the characteristic formulation for several time-dependent boundary conditions in favor of the Euler equations, and dropping the evolution equations for the physical grid coordinates over Ω in favor of algebraic expressions for the physical grid coordinates only at the body surface. Since the problem in Eqs. (7) and (8) consists of 12 equations and six unknowns, it is overconstrained. We are thus motivated to solve the problem in a least-squares sense. Each component of $\widehat{\mathbf{y}}(\xi,\eta)$, $\widehat{y}^q(\xi,\eta)$, $q=1,\ldots,6$, in Eqs. (7) and (8) is approximated by a truncated series expansion in the KL eigenfunctions, $\varphi_k^q(\xi,\eta)$, i.e.,

$$\widehat{y}^q(\xi,\eta)\approx\widetilde{y}^q(\xi,\eta)=\sum_{i=1}^{L}a_i^q\varphi_i^q(\xi,\eta),\quad q=1,\ldots,6,\ \ L\leqslant K, \tag{9}$$

so that the a_i^q, $i=1,\ldots,L$, $q=1,\ldots,6$, are the unknowns to be determined. Substituting the approximation $\widetilde{y}^q(\xi,\eta)$ from Eq. (9) into Eqs. (7) and (8), we get the following residual error function for $\widehat{\mathbf{f}}$, $\mathbf{e}_f$:

$$\mathbf{e}_f=\widehat{\mathbf{f}}\left(a_i^q,\varphi_i^q,\frac{\partial\varphi_i^q}{\partial\xi},\frac{\partial\varphi_i^q}{\partial\eta}\right),\quad q=1,\ldots,6,\ \ i=1,\ldots,L, \tag{10}$$

and the residual error function for $\widehat{\mathbf{g}}$, $\mathbf{e}_g$,

$$\mathbf{e}_g=\widehat{\mathbf{g}}\left(a_i^q,\varphi_i^q,\frac{\partial\varphi_i^q}{\partial\xi},\frac{\partial\varphi_i^q}{\partial\eta}\right),\quad q=1,\ldots,6,\ \ i=1,\ldots,L. \tag{11}$$

We now define the following weighted error:

$$e=\sum_{q=1}^{4}\omega_f^q\int_\Omega\sqrt{e_f^qe_f^q}\,\mathrm{d}\Omega+\sum_{q=1}^{8}\omega_g^q\int_S\sqrt{e_g^qe_g^q}\,\mathrm{d}S, \tag{12}$$

where e_f^q, $q=1,\ldots,4$, are the components of $\mathbf{e}_f$, and e_g^q, $q=1,\ldots,8$, are the components of $\mathbf{e}_g$. The approximation coefficients a_i^q in Eq. (9) are chosen in order to minimize e in Eq. (12). The ω_f^q and ω_g^q in Eq. (12) are constant weights which are chosen to enhance convergence to a global minimum for e. Since the problem of choosing an optimal set of weights ω_f^q and ω_g^q is difficult, for the current work, the weights were chosen by trial and error. The problem of minimizing e is a multi-variable minimization problem which is solved using a standard Newton method. The IMSL routine, DUMINF, is employed to minimize e in Eq. (12) for the current work.

3. Blunt body description and pseudospectral solver

Each of the three steps in developing a KL least-squares model of the Euler equations for the supersonic flow over a blunt body are now performed. We repeat essential portions of [2,4], which are needed for exposition of the KL technique.

3.1. Governing equations in physical coordinates

The two-dimensional, axisymmetric Euler equations for a calorically perfect ideal gas are, in dimensionless form:

$$\frac{\partial \rho}{\partial t} + u\frac{\partial \rho}{\partial r} + w\frac{\partial \rho}{\partial z} + \rho\left(\frac{\partial u}{\partial r} + \frac{\partial w}{\partial z} + \frac{u}{r}\right) = 0, \tag{13}$$

$$\frac{\partial u}{\partial t} + u\frac{\partial u}{\partial r} + w\frac{\partial u}{\partial z} + \frac{1}{\rho}\frac{\partial p}{\partial r} = 0, \tag{14}$$

$$\frac{\partial w}{\partial t} + u\frac{\partial w}{\partial r} + w\frac{\partial w}{\partial z} + \frac{1}{\rho}\frac{\partial p}{\partial z} = 0, \tag{15}$$

$$\frac{\partial p}{\partial t} + u\frac{\partial p}{\partial r} + w\frac{\partial p}{\partial z} + \gamma p\left(\frac{\partial u}{\partial r} + \frac{\partial w}{\partial z} + \frac{u}{r}\right) = 0, \tag{16}$$

where ρ is the density, p is the pressure, u and w are the velocities in the radial and axial directions, respectively, r is the radial coordinate, z is the axial coordinate, t is the time, and γ is the ratio of specific heats. The dimensional form for pressure, p^*, density, ρ^*, and r^* and z^* components of velocity, u^* and w^*, respectively, are recovered from the following equations:

$$p^* = pp^*_\infty, \tag{17}$$

$$\rho^* = \rho\rho^*_\infty, \tag{18}$$

$$u^* = u\sqrt{p^*_\infty/\rho^*_\infty}, \quad w^* = w\sqrt{p^*_\infty/\rho^*_\infty}, \tag{19}$$

where dimensional quantities are denoted by a $*$, and freestream quantities are denoted by ∞. The dimensional space and time variables are

$$z^* = zL^*, \quad r^* = rL^*, \tag{20}$$

$$t^* = tL^*/\sqrt{p^*_\infty/\rho^*_\infty}, \tag{21}$$

where L^* is the length of the body. The freestream flow is at zero angle of attack so that the component of freestream velocity in the r-direction, $u_\infty = 0$. Since the dimensionless pressure, p_∞, and density, ρ_∞, are equal to unity, the component of freestream velocity in the z-direction, w_∞, can be expressed as the following function of γ and the freestream Mach number, $\mathscr{M}_\infty$:

$$w_\infty = \sqrt{\gamma}\mathscr{M}_\infty. \tag{22}$$

Defining the entropy to be s, we have, for a calorically perfect ideal gas with zero freestream entropy,

$$s = \ln\left(\frac{p}{\rho^\gamma}\right), \tag{23}$$

where the entropy is non-dimensionalized by the specific heat at constant volume, c^*_v,

$$s^* = sc^*_v. \tag{24}$$

3.2. Computational and physical coordinates

The physical domain of the blunt body problem, Fig. 1, is mapped to the computational domain, $\xi \in [0,1]$, $\eta \in [0,1]$, in such a way that the body surface lies along the computational boundary $(\xi, 0)$, the shock lies along the boundary $(\xi, 1)$, the symmetry axis is a third boundary at $(0, \eta)$, and the fourth boundary at $(1, \eta)$ is a supersonic outflow. The transformation between the physical coordinates (r, z) and computational coordinates (ξ, η) is taken to be

$$r(\xi,\eta,\tau) = R(\xi) + \frac{\eta \frac{\mathrm{d}Z(\xi)}{\mathrm{d}\xi} h(\xi,\tau)}{\sqrt{\left(\frac{\mathrm{d}R(\xi)}{\mathrm{d}\xi}\right)^2 + \left(\frac{\mathrm{d}Z(\xi)}{\mathrm{d}\xi}\right)^2}}, \tag{25}$$

$$z(\xi,\eta,\tau) = Z(\xi) - \frac{\eta \frac{\mathrm{d}R(\xi)}{\mathrm{d}\xi} h(\xi,\tau)}{\sqrt{\left(\frac{\mathrm{d}R(\xi)}{\mathrm{d}\xi}\right)^2 + \left(\frac{\mathrm{d}Z(\xi)}{\mathrm{d}\xi}\right)^2}}, \tag{26}$$

where the nonlinear function $h(\xi, \tau)$ must be specified to completely determine the mapping and $R(\xi)$ and $Z(\xi)$ are known functions. After manipulation, the transformations in Eqs. (25) and (26) yield the following identity:

$$h(\xi,\tau) = \sqrt{(z(\xi,1,\tau) - z(\xi,0,\tau))^2 + (r(\xi,1,\tau) - r(\xi,0,\tau))^2}, \tag{27}$$

from which it is seen that $h(\xi, \tau)$ is the distance in $r - z$ space between the body surface, $\eta = 0$, and the shock, $\eta = 1$, along lines of constant ξ. We see that Eqs. (25) and (26) form an implicit algebraic equation for the coordinate transformation. It is apparent from Eqs. (25) and (26) that the functions $R(\xi)$ and $Z(\xi)$ parameterize the blunt body surface, $\eta = 0$, i.e.,

$$r(\xi,0,\tau) = R(\xi), \tag{28}$$

$$z(\xi,0,\tau) = Z(\xi), \tag{29}$$

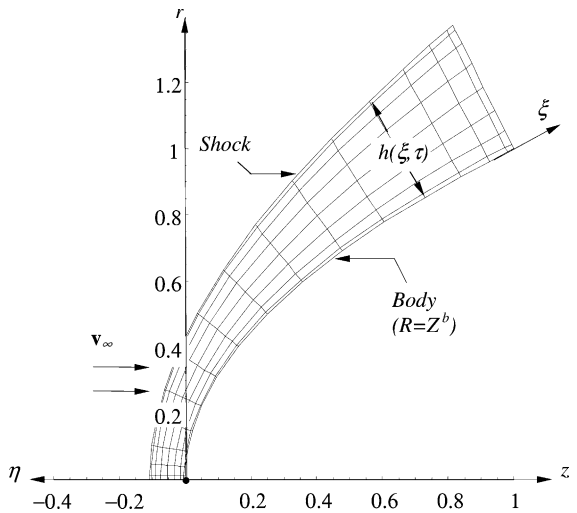

Fig. 1. Schematic of shock-fitted high Mach number flow over an axisymmetric blunt body including computational (ξ, η) and physical (r, z) coordinates.

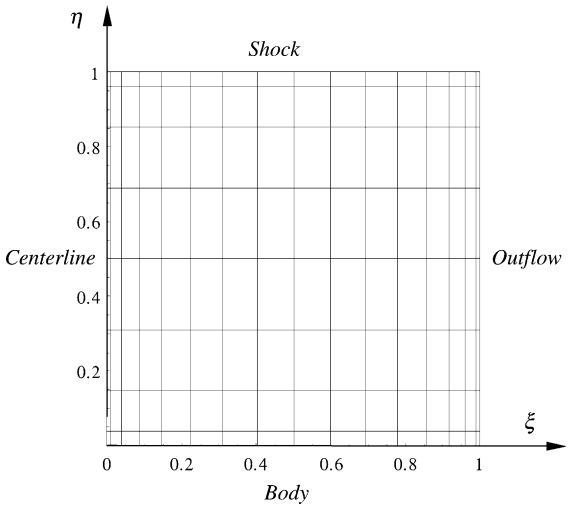

Fig. 2. Gauss–Lobatto Chebyshev computational grid for the shock-fitted blunt body.

and that the body surface is not a function of time. The transformations in Eqs. (25) and (26) have been constructed so that lines of constant ξ are normal to the body surface and have no curvature in $r-z$ space. The computational grid is shown in Fig. 2, where the nodes in the ξ and η directions correspond to the location of the zeroes of a Chebyshev polynomial of order N and M respectively. This choice of nodes is not unique and is made because global Lagrange polynomial approximations of general non-periodic functions defined on this grid were found in Brooks [2] to yield a more uniform and overall lower error than a uniform grid. For the current problem, we have chosen the following functions to parameterize the blunt body surface:

$$R(\xi) = \xi, \tag{30}$$

$$Z(\xi) = \xi^{1/b}, \tag{31}$$

where the domain for the geometric parameter b is restricted to $b \in (0,1)$.

3.3. Governing equations and boundary conditions in computational coordinates

After transforming the Euler equations, zero mass flux boundary condition at the body surface, $\eta = 0$, Rankine–Hugoniot relations at the shock boundary, $\eta = 1$, supersonic outflow condition at $\xi = 1$, and centerline boundary conditions at $\xi = 0$, from $r-z$ space to $\xi-\eta$ space, the governing equations and boundary conditions can be expressed in the form of Eqs. (2) and (3), where

$$\mathbf{y}(\xi,\eta,\tau) = \begin{bmatrix} \rho(\xi,\eta,\tau) \\ u(\xi,\eta,\tau) \\ w(\xi,\eta,\tau) \\ p(\xi,\eta,\tau) \\ r(\xi,\eta,\tau) \\ z(\xi,\eta,\tau) \\ v_{\mathrm{BT}}(\xi,\tau) \\ \rho(\xi,0,\tau) \\ p(\xi,0,\tau) \\ v(\xi,\tau) \end{bmatrix}, \tag{32}$$

$$
\mathbf{f} = \begin{bmatrix}
-\widehat{u}\dfrac{\partial \rho}{\partial \xi} - \widehat{w}\dfrac{\partial \rho}{\partial \eta} - \rho\left(\dfrac{\partial \xi}{\partial r}\dfrac{\partial u}{\partial \xi} + \dfrac{\partial \xi}{\partial z}\dfrac{\partial w}{\partial \xi} + \dfrac{\partial \eta}{\partial r}\dfrac{\partial u}{\partial \eta} + \dfrac{\partial \eta}{\partial z}\dfrac{\partial w}{\partial \eta}\right) - \dfrac{\rho u}{r} \\
-\widehat{u}\dfrac{\partial u}{\partial \xi} - \widehat{w}\dfrac{\partial u}{\partial \eta} - \dfrac{1}{\rho}\left(\dfrac{\partial \xi}{\partial r}\dfrac{\partial p}{\partial \xi} + \dfrac{\partial \eta}{\partial r}\dfrac{\partial p}{\partial \eta}\right) \\
-\widehat{u}\dfrac{\partial w}{\partial \xi} - \widehat{w}\dfrac{\partial w}{\partial \eta} - \dfrac{1}{\rho}\left(\dfrac{\partial \xi}{\partial z}\dfrac{\partial p}{\partial \xi} + \dfrac{\partial \eta}{\partial z}\dfrac{\partial p}{\partial \eta}\right) \\
-\widehat{u}\dfrac{\partial p}{\partial \xi} - \widehat{w}\dfrac{\partial p}{\partial \eta} - \gamma p\left(\dfrac{\partial \xi}{\partial r}\dfrac{\partial u}{\partial \xi} + \dfrac{\partial \xi}{\partial z}\dfrac{\partial w}{\partial \xi} + \dfrac{\partial \eta}{\partial r}\dfrac{\partial u}{\partial \eta} + \dfrac{\partial \eta}{\partial z}\dfrac{\partial w}{\partial \eta}\right) - \dfrac{\gamma p u}{r} \\
\dfrac{\eta \dfrac{\partial Z(\xi)}{\partial \xi} v(\xi,\tau)}{\sqrt{\left(\dfrac{\partial R(\xi)}{\partial \xi}\right)^2 + \left(\dfrac{\partial Z(\xi)}{\partial \xi}\right)^2}} \\
-\dfrac{\eta \dfrac{\partial R(\xi)}{\partial \xi} v(\xi,\tau)}{\sqrt{\left(\dfrac{\partial R(\xi)}{\partial \xi}\right)^2 + \left(\dfrac{\partial Z(\xi)}{\partial \xi}\right)^2}} \\
-\left.\dfrac{\left[\widehat{u}\left(\dfrac{\partial \eta}{\partial r}\dfrac{\partial w}{\partial \xi} - \dfrac{\partial \eta}{\partial z}\dfrac{\partial u}{\partial \xi}\right) + \dfrac{1}{\rho}\left(\dfrac{\partial \eta}{\partial r}\dfrac{\partial \xi}{\partial z} - \dfrac{\partial \eta}{\partial z}\dfrac{\partial \xi}{\partial r}\right)\dfrac{\partial p}{\partial \xi}\right]}{\sqrt{\left(\dfrac{\partial \eta}{\partial z}\right)^2 + \left(\dfrac{\partial \eta}{\partial r}\right)^2}}\right|_{(\xi,0,\tau)} \\
\left.\left[-\dfrac{1}{c^2}\dfrac{\partial p}{\partial \tau} + \widehat{u}\left(\dfrac{\partial \rho}{\partial \xi} - \dfrac{1}{c^2}\dfrac{\partial p}{\partial \xi}\right)\right]\right|_{(\xi,0,\tau)} \\
-\left.\left[\dfrac{\rho c \widehat{u}\left(\dfrac{\partial \eta}{\partial r}\dfrac{\partial u}{\partial \xi} + \dfrac{\partial \eta}{\partial z}\dfrac{\partial w}{\partial \xi}\right) + c\left(\dfrac{\partial \eta}{\partial r}\dfrac{\partial \xi}{\partial r} + \dfrac{\partial \eta}{\partial z}\dfrac{\partial \xi}{\partial z}\right)\dfrac{\partial p}{\partial \xi}}{\sqrt{\left(\dfrac{\partial \eta}{\partial z}\right)^2 + \left(\dfrac{\partial \eta}{\partial r}\right)^2}}\right.\right. \\
-\rho c^2\left(\dfrac{\partial \xi}{\partial r}\dfrac{\partial u}{\partial \xi} + \dfrac{\partial \xi}{\partial z}\dfrac{\partial w}{\partial \xi} + \dfrac{\partial \eta}{\partial r}\dfrac{\partial u}{\partial \eta} + \dfrac{\partial \eta}{\partial z}\dfrac{\partial w}{\partial \eta}\right) \\
\left.\left.+c\sqrt{\left(\dfrac{\partial \eta}{\partial z}\right)^2 + \left(\dfrac{\partial \eta}{\partial r}\right)^2}\dfrac{\partial p}{\partial \eta} - \widehat{u}\dfrac{\partial p}{\partial \xi} - \dfrac{\rho c^2 u}{r}\right]\right|_{(\xi,0,\tau)} \\
-\left.\left[\dfrac{(A_2 + \rho c A_1)(\mathbf{v}_\infty - v\mathbf{e}_\eta)\cdot\dfrac{\partial \mathbf{e}_{SN}}{\partial \tau} - \rho c(\mathbf{v} - v\mathbf{e}_\eta)\cdot\dfrac{\partial \mathbf{e}_{SN}}{\partial \tau} + A_3}{(\mathbf{e}_\eta \cdot \mathbf{e}_{SN})[A_2 + \rho c(A_1 - 1)]}\right]\right|_{(\xi,1,\tau)}
\end{bmatrix}, \tag{33}
$$

$$\mathbf{g} = \begin{bmatrix} \left[u - \dfrac{v_{\mathrm{BT}} \dfrac{\partial r}{\partial \xi}}{\sqrt{\left(\dfrac{\partial r}{\partial \xi}\right)^2 + \left(\dfrac{\partial z}{\partial \xi}\right)^2}} \right]\Bigg|_{(\xi,0,\tau)} \\ \left[w - \dfrac{v_{\mathrm{BT}} \dfrac{\partial z}{\partial \xi}}{\sqrt{\left(\dfrac{\partial r}{\partial \xi}\right)^2 + \left(\dfrac{\partial z}{\partial \xi}\right)^2}} \right]\Bigg|_{(\xi,0,\tau)} \\ \rho(\xi,1,\tau) - \dfrac{\delta_\infty(\xi,\tau)}{\delta_S(\xi,\tau)} \\ \left[\mathbf{v}_\infty \cdot \mathbf{e}_{\mathrm{ST}} - \mathbf{v} \cdot \mathbf{e}_{\mathrm{ST}}\right]|_{(\xi,1,\tau)} \\ \delta_S(\xi,\tau) - \dfrac{\gamma-1}{\gamma+1}\delta_\infty(\xi,\tau) + \dfrac{2\gamma}{(\gamma+1)\delta_\infty(\xi,\tau)} \\ p(\xi,1,\tau) - \dfrac{2}{\gamma+1}\delta_\infty^2(\xi,\tau) - \dfrac{\gamma-1}{\gamma+1} \\ \rho(0,\eta,\tau) - \rho(0,1,\tau)\left(\dfrac{p(0,\eta,\tau)}{p(0,1,\tau)}\right)^{1/\gamma} \\ u(0,\eta,\tau) \\ \left.\dfrac{\partial w}{\partial \xi}\right|_{(0,\eta,\tau)} \\ \left.\dfrac{\partial p}{\partial \xi}\right|_{(0,\eta,\tau)} \\ \left.\dfrac{\partial v}{\partial \xi}\right|_{(0,\tau)} \end{bmatrix}. \tag{34}$$

In Eqs. (32) and (33), the first equation is the continuity equation, the second and third equations are the ξ and η momentum equations, the fourth is the energy equation, the fifth and sixth are the r and z grid evolution equations, the seventh, eighth and ninth equations are the characteristic equations for tangential velocity, density, and pressure, respectively, at the boundary, $\eta = 0$, and the 10th equation is the shock acceleration equation. The algebraic equations in Eq. (34) are the remaining boundary conditions necessary for a well-posed problem. The contravariant velocity components $\widehat{u}$ and $\widehat{w}$ in Eqs. (32)–(34) are:

$$\begin{aligned} \widehat{u} &= \frac{\partial \xi}{\partial t} + u\frac{\partial \xi}{\partial r} + w\frac{\partial \xi}{\partial z}, \\ \widehat{w} &= \frac{\partial \eta}{\partial t} + u\frac{\partial \eta}{\partial r} + w\frac{\partial \eta}{\partial z}, \end{aligned} \tag{35}$$

$c = \sqrt{\gamma p/\rho}$ is the dimensionless acoustic speed, v_{BT} is the velocity component tangent to the body surface, and v is the component of the shock velocity in the η-direction. The vectors $\mathbf{e}_\eta$, $\mathbf{e}_{\mathrm{ST}}$, and $\mathbf{e}_{\mathrm{SN}}$ are the unit vectors in the η, shock tangent, and shock normal directions, respectively, defined as follows:

$$\mathbf{e}_\eta = \frac{\left(\dfrac{\mathrm{d}Z(\xi)}{\mathrm{d}\xi}\mathbf{e}_r - \dfrac{\mathrm{d}R(\xi)}{\mathrm{d}\xi}\mathbf{e}_z\right)}{\sqrt{\left(\dfrac{\mathrm{d}Z(\xi)}{\mathrm{d}\xi}\right)^2 + \left(\dfrac{\mathrm{d}R(\xi)}{\mathrm{d}\xi}\right)^2}}, \tag{36}$$

$$\mathbf{e}_{\mathrm{ST}} = \left.\frac{-\dfrac{\partial\eta}{\partial z}\mathbf{e}_r + \dfrac{\partial\eta}{\partial r}\mathbf{e}_z}{\sqrt{\left(\dfrac{\partial\eta}{\partial z}\right)^2 + \left(\dfrac{\partial\eta}{\partial r}\right)^2}}\right|_{(\xi,1,\tau)}, \tag{37}$$

$$\mathbf{e}_{\mathrm{SN}} = \left.\frac{\dfrac{\partial\eta}{\partial r}\mathbf{e}_r + \dfrac{\partial\eta}{\partial z}\mathbf{e}_z}{\sqrt{\left(\dfrac{\partial\eta}{\partial z}\right)^2 + \left(\dfrac{\partial\eta}{\partial r}\right)^2}}\right|_{(\xi,1,\tau)}, \tag{38}$$

where $\mathbf{e}_r$ and $\mathbf{e}_z$ are the unit vectors in the r and z directions, respectively. The velocity vector is defined as

$$\mathbf{v} = u\mathbf{e}_r + w\mathbf{e}_z, \tag{39}$$

so that, from Eq. (22), the freestream velocity vector is

$$\mathbf{v}_\infty = \sqrt{\gamma}\mathscr{M}_\infty\mathbf{e}_z. \tag{40}$$

The functions, δ_S, δ_∞, A_1, A_2, and A_3 are

$$\delta_S(\xi,\tau) = \mathbf{v}\cdot\mathbf{e}_{\mathrm{SN}}|_{(\xi,1,\tau)} - \left(\mathbf{e}_\eta\cdot\mathbf{e}_{\mathrm{SN}}\right)v(\xi,\tau), \tag{41}$$

$$\delta_\infty(\xi,\tau) = \mathbf{v}_\infty\cdot\mathbf{e}_{\mathrm{SN}}|_{(\xi,1,\tau)} - \left(\mathbf{e}_\eta\cdot\mathbf{e}_{\mathrm{SN}}\right)v(\xi,\tau), \tag{42}$$

$$A_1(\xi,\tau) = \frac{\gamma-1}{\gamma+1} - \frac{2\gamma}{(\gamma+1)\delta_\infty^2(\xi,\tau)}, \quad A_2(\xi,\tau) = \frac{4\delta_\infty(\xi,\tau)}{\gamma+1}, \tag{43}$$

$$\begin{aligned} A_3 = {} & \widehat{u}\frac{\partial p}{\partial\xi} + \widehat{w}\frac{\partial p}{\partial\eta} + \gamma p\left(\frac{\partial\xi}{\partial z}\frac{\partial w}{\partial\xi} + \frac{\partial\eta}{\partial z}\frac{\partial w}{\partial\eta} + \frac{\partial\xi}{\partial r}\frac{\partial u}{\partial\xi} + \frac{\partial\eta}{\partial r}\frac{\partial u}{\partial\eta}\right)\rho c\left[\frac{\dfrac{\partial z}{\partial\xi}}{\sqrt{\left(\dfrac{\partial z}{\partial\xi}\right)^2 + \left(\dfrac{\partial r}{\partial\xi}\right)^2}}\left(\widehat{u}\frac{\partial u_r}{\partial\xi} + \widehat{w}\frac{\partial u}{\partial\eta}\right.\right. \\ & \left.\left. + \frac{1}{\rho}\left(\frac{\partial\xi}{\partial r}\frac{\partial p}{\partial\xi} + \frac{\partial\eta}{\partial r}\frac{\partial p}{\partial\eta}\right)\right) - \frac{\dfrac{\partial r}{\partial\xi}}{\sqrt{\left(\dfrac{\partial z}{\partial\xi}\right)^2 + \left(\dfrac{\partial r}{\partial\xi}\right)^2}}\left(\widehat{u}\frac{\partial w}{\partial\xi} + \widehat{w}\frac{\partial w}{\partial\eta} + \frac{1}{\rho}\left(\frac{\partial\xi}{\partial z}\frac{\partial p}{\partial\xi} + \frac{\partial\eta}{\partial z}\frac{\partial p}{\partial\eta}\right)\right)\right] + \frac{\gamma p u}{r}. \end{aligned} \tag{44}$$

Finally, the following standard relations between the metrics and inverse metrics will be necessary in formulating the least-squares KL model,

$$\begin{aligned} &\frac{\partial\xi}{\partial z} = \frac{1}{J}\frac{\partial r}{\partial\eta}, \quad \frac{\partial\eta}{\partial z} = -\frac{1}{J}\frac{\partial r}{\partial\xi}, \\ &\frac{\partial\xi}{\partial r} = -\frac{1}{J}\frac{\partial z}{\partial\eta}, \quad \frac{\partial\eta}{\partial r} = \frac{1}{J}\frac{\partial z}{\partial\xi}, \\ &\frac{\partial\xi}{\partial t} = \frac{\left(\dfrac{\partial r}{\partial\tau}\dfrac{\partial z}{\partial\eta} - \dfrac{\partial r}{\partial\eta}\dfrac{\partial z}{\partial\tau}\right)}{J}, \quad \frac{\partial\eta}{\partial t} = \frac{\left(\dfrac{\partial r}{\partial\xi}\dfrac{\partial z}{\partial\tau} - \dfrac{\partial r}{\partial\tau}\dfrac{\partial z}{\partial\xi}\right)}{J}, \\ &J = \frac{\partial r}{\partial\eta}\frac{\partial z}{\partial\xi} - \frac{\partial r}{\partial\xi}\frac{\partial z}{\partial\eta}, \end{aligned} \tag{45}$$

where J is the determinant of the metric Jacobian matrix.

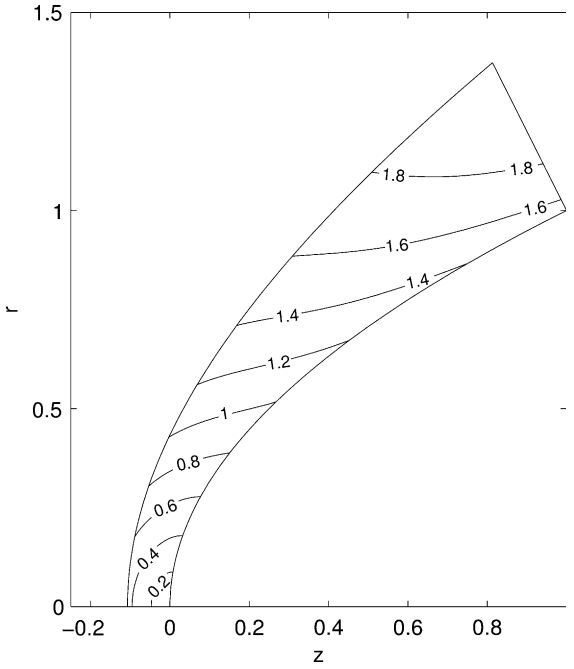

Fig. 3. Contours of Mach number for flow over the blunt body for $b = 0.5$, $\mathscr{M}_\infty = 3.5$, 17×9 grid.

3.4. Pseudospectral numerical technique and solutions

In order to solve the system of partial differential-algebraic equations in Eqs. (32)–(34), the spatial derivatives ρ, u, w, p, r, and z are approximated in terms of global Lagrange interpolating polynomials defined on the grid points (ξ_i, η_j), $i = 0, \ldots, N$, $j = 0, \ldots, M$, thus Eqs. (32)–(34) are reduced to a system of ordinary differential-algebraic equations. Furthermore, by deriving explicit expressions for the algebraic variables in terms of the differential variables, the system of differential algebraic equations is converted into a system of ODEs which are then solved using a standard ODE solver. Contours of Mach number are shown in Fig. 3. The sonic line, $\mathscr{M} = 1$, is predicted in Fig. 3 as well as the fact that the outflow velocity is indeed supersonic as required in the derivation of the outflow boundary condition. Further details of the numerical method can be found in [2,4] along with code verification and validation.

4. Blunt body KL modes

Ten solutions, also referred to as snapshots in the context of the KL method, are generated for 10 different values of $\mathscr{M}_\infty$ chosen uniformly in the range $\mathscr{M}_\infty \in [3, 4]$, with the geometric parameter b fixed at 0.5. From these 10 snapshots, 10 KL modes, φ_k^q and associated eigenvalues λ_k^q, $k = 1, \ldots, 10$, $q = 1, \ldots, 6$, are calculated for each of the primitive variables, ρ, u, w, and p and the physical coordinates r and z, where subscripts indicate the number of the mode and superscripts dictate to which variable the KL modes and eigenvalues belong. The method of snapshots, Sirovich [38], was used to generate the KL modes and eigenvalues. A plot of the eigenvalues of density as a function of KL mode number are shown in Fig. 4, while the 10 normalized KL modes are shown in Fig. 5. A rapid decay in the magnitude of the eigenvalues and a progressively richer topologically structured set of KL modes is observed as the mode number increases.

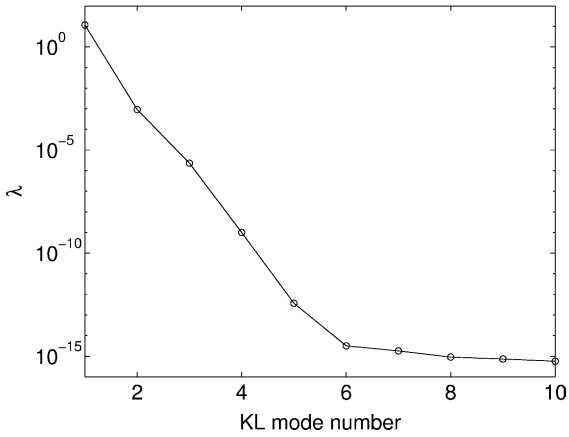

Fig. 4. Eigenvalues of density for 10 snapshots over the range $\mathscr{M}_\infty \in [3,4]$.

5. Least-squares method

In the KL least-squares method, the steady-state density, $\widetilde{\rho}(\xi,\eta)$, r and z velocity components, $\widetilde{u}(\xi,\eta)$ and $\widetilde{w}(\xi,\eta)$, respectively, pressure, $\widetilde{p}(\xi,\eta)$, and physical grid coordinates $\widetilde{r}(\xi,\eta)$ and $\widetilde{z}(\xi,\eta)$ are approximated in terms of the KL modes as follows,

$$\begin{aligned}
\widetilde{\rho}(\xi,\eta) &= \sum_{k=1}^{K} a_k^1 \varphi_k^1(\xi,\eta),\\
\widetilde{u}(\xi,\eta) &= \sum_{k=1}^{K} a_k^2 \varphi_k^2(\xi,\eta),\\
\widetilde{w}(\xi,\eta) &= \sum_{k=1}^{K} a_k^3 \varphi_k^3(\xi,\eta),\\
\widetilde{p}(\xi,\eta) &= \sum_{k=1}^{K} a_k^4 \varphi_k^4(\xi,\eta),\\
\widetilde{r}(\xi,\eta) &= \sum_{k=1}^{K} a_k^5 \varphi_k^5(\xi,\eta),\\
\widetilde{z}(\xi,\eta) &= \sum_{k=1}^{K} a_k^6 \varphi_k^6(\xi,\eta).
\end{aligned} \tag{46}$$

Employing Eq. (46), the KL least-squares formulation of the blunt body problem is written in the form of Eqs. (10) and (11), where

$$\widehat{\mathbf{f}}\left(a_i^q, \varphi_i^q, \frac{\partial \varphi_i^q}{\partial \xi}, \frac{\partial \varphi_i^q}{\partial \eta}\right) = \begin{bmatrix}
\widehat{\widetilde{u}}\dfrac{\partial \widetilde{u}}{\partial \xi} + \widehat{\widetilde{w}}\dfrac{\partial \widetilde{u}}{\partial \eta} + \dfrac{1}{\widetilde{\rho}}\left(\dfrac{\partial \xi}{\partial \widetilde{r}}\dfrac{\partial \widetilde{p}}{\partial \xi} + \dfrac{\partial \eta}{\partial \widetilde{r}}\dfrac{\partial \widetilde{p}}{\partial \eta}\right)\\
\widehat{\widetilde{u}}\dfrac{\partial \widetilde{w}}{\partial \xi} + \widehat{\widetilde{w}}\dfrac{\partial \widetilde{w}}{\partial \eta} + \dfrac{1}{\widetilde{\rho}}\left(\dfrac{\partial \xi}{\partial \widetilde{z}}\dfrac{\partial \widetilde{p}}{\partial \xi} + \dfrac{\partial \eta}{\partial \widetilde{z}}\dfrac{\partial \widetilde{p}}{\partial \eta}\right)\\
\widehat{\widetilde{u}}\dfrac{\partial p}{\partial \xi} - \widehat{\widetilde{w}}\dfrac{\partial p}{\partial \eta} - \gamma\widetilde{p}\left(\dfrac{\partial \xi}{\partial \widetilde{r}}\dfrac{\partial \widetilde{u}}{\partial \xi} + \dfrac{\partial \xi}{\partial \widetilde{z}}\dfrac{\partial \widetilde{w}}{\partial \xi} + \dfrac{\partial \eta}{\partial \widetilde{r}}\dfrac{\partial \widetilde{u}}{\partial \eta} + \dfrac{\partial \eta}{\partial \widetilde{z}}\dfrac{\partial \widetilde{w}}{\partial \eta}\right) - \dfrac{\gamma\widetilde{p}\widetilde{u}}{\widetilde{r}}\\
\widehat{\widetilde{u}}\dfrac{\partial \widetilde{\rho}}{\partial \xi} - \widehat{\widetilde{w}}\dfrac{\partial \widetilde{\rho}}{\partial \eta} - \widetilde{\rho}\left(\dfrac{\partial \xi}{\partial \widetilde{r}}\dfrac{\partial \widetilde{u}}{\partial \xi} + \dfrac{\partial \xi}{\partial \widetilde{z}}\dfrac{\partial \widetilde{w}}{\partial \xi} + \dfrac{\partial \eta}{\partial \widetilde{r}}\dfrac{\partial \widetilde{u}}{\partial \eta} + \dfrac{\partial \eta}{\partial \widetilde{z}}\dfrac{\partial \widetilde{w}}{\partial \eta}\right) - \dfrac{\widetilde{\rho}\widetilde{u}}{\widetilde{r}}
\end{bmatrix} \tag{47}$$

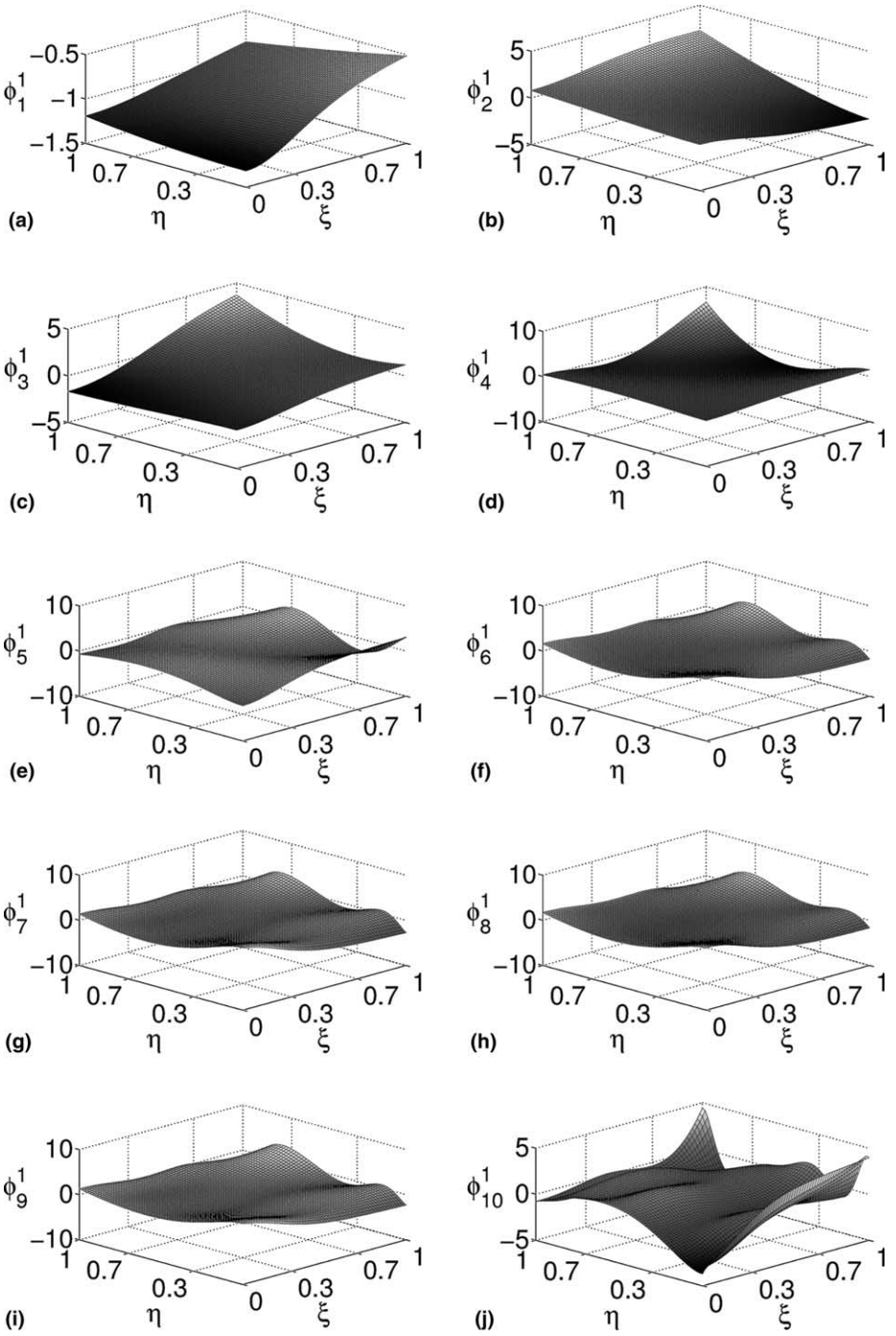

Fig. 5. Ten KL eigenmodes of density with associated eigenvalues, λ, generated from 10 snapshots in the range $\mathscr{M}_\infty \in [3,4]$. (a) $\lambda_1 = 11.4$, (b) $\lambda_2 = 9.16 \times 10^{-4}$, (c) $\lambda_3 = 2.28 \times 10^{-6}$, (d) $\lambda_4 = 1.03 \times 10^{-9}$, (e) $\lambda_5 = 3.70 \times 10^{-13}$, (f) $\lambda_6 = 2.48 \times 10^{-15}$, (g) $\lambda_7 = 2.38 \times 10^{-15}$, (h) $\lambda_8 = 1.02 \times 10^{-15}$, (i) $\lambda_9 = 7.56 \times 10^{-16}$ and (j) $\lambda_{10} = 3.52 \times 10^{-16}$.

and

$$\widehat{\mathbf{g}}\left(a_i^q, \varphi_i^q, \frac{\partial \varphi_i^q}{\partial \xi}, \frac{\partial \varphi_i^q}{\partial \eta}\right) = \begin{bmatrix} \widetilde{v}_{\mathrm{BN}}(\xi) \\ [\mathbf{v}_\infty \cdot \widetilde{\mathbf{e}}_{\mathrm{ST}} - \widetilde{\mathbf{v}} \cdot \widetilde{\mathbf{e}}_{\mathrm{ST}}]|_{(\xi,1)} \\ \left[\widetilde{\delta} - \dfrac{\gamma-1}{\gamma+1}\widetilde{\delta}_\infty + \dfrac{2\gamma}{(\gamma+1)\widetilde{\delta}_\infty}\right]\Big|_{(\xi,1)} \\ \left[\widetilde{p} - \dfrac{2}{\gamma+1}\widetilde{\delta}_\infty^2 - \dfrac{\gamma-1}{\gamma+1}\right]\Big|_{(\xi,1)} \\ \left[\widetilde{\rho} - \dfrac{\widetilde{\delta}_\infty}{\widetilde{\delta}}\right]\Big|_{(\xi,1)} \\ \widetilde{\rho}(0,\eta,\tau) - \widetilde{\rho}(0,1,\tau)\left(\dfrac{\widetilde{p}(0,\eta,\tau)}{\widetilde{p}(0,1,\tau)}\right)^{1/\gamma} \\ \widetilde{r}(\xi,0) - r(\xi,0) \\ \widetilde{z}(\xi,0) - z(\xi,0) \end{bmatrix}, \tag{48}$$

where

$$\widetilde{\delta} = \widetilde{\mathbf{v}} \cdot \widetilde{\mathbf{e}}_{\mathrm{SN}}|_{(\xi,1)}, \tag{49}$$

$$\widetilde{\delta}_\infty = \mathbf{v}_\infty \cdot \widetilde{\mathbf{e}}_{\mathrm{SN}}|_{(\xi,1)}, \tag{50}$$

$$\widetilde{v}_{\mathrm{BN}}(\xi) = \left(\widetilde{u}\frac{\partial \widetilde{z}}{\partial \xi} - \widetilde{w}\frac{\partial \widetilde{r}}{\partial \xi}\right)\Big|_{(\xi,0)}, \tag{51}$$

$$\widehat{\widetilde{u}} = \widetilde{u}\frac{\partial \xi}{\partial \widetilde{r}} + \widetilde{w}\frac{\partial \xi}{\partial \widetilde{z}}, \tag{52}$$

$$\widehat{\widetilde{w}} = \widetilde{u}\frac{\partial \eta}{\partial \widetilde{r}} + \widetilde{w}\frac{\partial \eta}{\partial \widetilde{z}}. \tag{53}$$

The approximate metric terms

$$\frac{\partial \xi}{\partial \widetilde{r}}, \quad \frac{\partial \xi}{\partial \widetilde{z}}, \quad \frac{\partial \eta}{\partial \widetilde{r}} \quad \text{and} \quad \frac{\partial \eta}{\partial \widetilde{z}}$$

are found from the inverse metrics in Eq. (45) and the relations in Eq. (46), e.g.,

$$\frac{\partial \xi}{\partial \widetilde{r}} = -\frac{1}{J}\frac{\partial \widetilde{z}}{\partial \eta}.$$

The spatial derivatives in Eq. (47) are calculated by taking derivatives of the quantities in Eq. (46), e.g.,

$$\frac{\partial}{\partial \xi}\widetilde{\rho}(\xi,\eta) = \sum_{k=1}^{K} a_k^1 \frac{\partial}{\partial \xi}\varphi_k^1(\xi,\eta), \quad \frac{\partial}{\partial \eta}\widetilde{\rho}(\xi,\eta) = \sum_{k=1}^{K} a_k^1 \frac{\partial}{\partial \eta}\varphi_k^1(\xi,\eta). \tag{54}$$

The terms $\widetilde{\mathbf{e}}_{\mathrm{ST}}$ and $\widetilde{\mathbf{e}}_{\mathrm{SN}}$ in Eqs. (48)–(50) are found by substituting the KL approximations for the metrics $\partial\eta/\partial\widetilde{r}$ and $\partial\eta/\partial\widetilde{z}$ into Eqs. (37) and (38). In Eq. (48), the coordinates $r(\xi,0)$ and $z(\xi,0)$ are specified from

the choice of b which fixes the body surface via the parameterization in Eqs. (30) and (31). The linear boundary conditions in Eq. (34),

$$\left.\frac{\partial w}{\partial \xi}\right|_{(0,\eta,\tau)} = 0, \quad \left.\frac{\partial p}{\partial \xi}\right|_{(0,\eta,\tau)} = 0, \quad u|_{(0,\eta,\tau)} = 0, \quad \left.\frac{\partial z}{\partial \xi}\right|_{(0,\eta,\tau)} = 0, \quad \text{and} \quad r|_{(0,\eta,\tau)} = 0$$

are not included in Eq. (48), since each of the KL modes satisfies them exactly; this is apparent upon noting that the KL modes are linear combinations of the snapshots, Sirovich [38]. In addition, at steady state we have $v(\xi,\tau) = 0$, so that the evolution equations for physical grid coordinates and the equation for the shock velocity in Eqs. (32) and (33) are not considered. The physical grid coordinates over the domain Ω are included implicitly in the functions $\widehat{\mathbf{f}}$ and $\widehat{\mathbf{g}}$ through the metrics and explicitly in the last two components of $\widehat{\mathbf{g}}$ at the body surface, $\eta = 0$.

We define the following error functions over the domain Ω:

$$e_f^q = \widehat{f}^q, \quad q = 1,\ldots,4, \tag{55}$$

where $\widehat{f}^q$ is the qth component of the function $\widehat{\mathbf{f}}$. At the boundary S, the error function is defined as:

$$e_g^q = \widehat{g}^q, \quad q = 1,\ldots,8, \tag{56}$$

where $\widehat{g}^q$ is the qth component of $\widehat{\mathbf{g}}$. A total error, e, is formed from Eqs. (55) and (56) as follows:

$$e = \sum_{q=1}^{4} \int_\Omega \omega_f^q \sqrt{e_f^q e_f^q}\, \mathrm{d}\Omega + \sum_{q=1}^{8} \int_S \omega_g^q \sqrt{e_g^q e_g^q}\, \mathrm{d}S, \tag{57}$$

where $\omega_f^q = \omega_g^q = 1$, $q = 1,\ldots,3$, $\omega_f^4 = \omega_g^4 = 0.1$, $\omega_g^5 = \omega_g^6 = 1$, and $\omega_g^7 = \omega_g^8 = 1000$ are constant weights chosen to enhance convergence to a global minimum for e. The coefficients in Eq. (46) are chosen via a Newton method such that the total error, e defined in Eq. (57), is minimized. Due to the nature of the nonlinearity in the functions e_f^q and e_g^q in Eq. (57), it is not possible to factor the coefficients, a_k^q, $q = 1,\ldots,6$, $k = 1,\ldots,L$, outside of the integral operator; consequently, whenever one of the coefficients changes, the integrals must be reevaluated to determine e. This is different from the work by other researchers such as Park and Jung [16], where the nonlinearities in the problem were such that the coefficients could be factored outside the integrals. As a consequence, for Park and Jung, the integrals could be evaluated once and for all at the time of model construction since the functions φ_i^q, $\partial\varphi_i^q/\partial\xi$, and $\partial\varphi_i^q/\partial\eta$, $q = 1,\ldots,6$, $k = 1,\ldots,L$, are all known once the KL decomposition has been performed.

6. Results for KL least-squares model for supersonic blunt body flow

6.1. Error convergence for 10 snapshot KL model, $\mathscr{M}_\infty \in [3,4]$, $b = 1/2$

Convergence of the $L_\infty[\Omega]$ error in $\rho(\xi,\eta)$ as a function of the number of KL modes is shown in Fig. 6 for a KL model built from 10 snapshots. The 10 snapshots are uniformly distributed over the range $\mathscr{M}_\infty \in [3,4]$, while the geometry is fixed at $b = 0.5$. The snapshots are generated using the pseudospectral solver described in [2,4] on both a 17×9 grid and a 22×12 grid. The error is assessed by comparison with a highly resolved 33×17 grid solution. After the fourth mode for the 17×9 grid KL model and after the fifth mode for the 22×12 grid KL model, there is no further improvement in the accuracy of the model, since the KL model accuracy has reached the level of error in the samples as shown by the dark lines in Fig. 6.

The distribution of $L_\infty[\Omega]$ error in $\rho(\xi,\eta)$ for the KL model over the entire range, $\mathscr{M}_\infty \in [3,4]$, is shown in Fig. 7 for the KL model built from 10 17×9 grid pseudospectral snapshots. Once again, the $L_\infty[\Omega]$ error

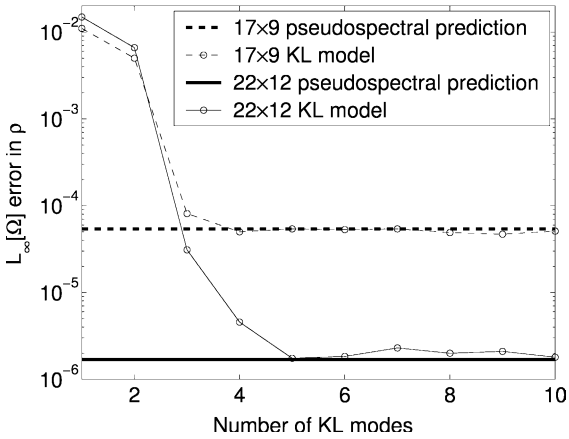

Fig. 6. KL model $L_\infty[\Omega]$ error in ρ for both a 17×9 and 22×12 grid, $\mathscr{M}_\infty = 3.5, b = 0.5$. A highly resolved 33×17 grid solution is the standard for the reported errors.

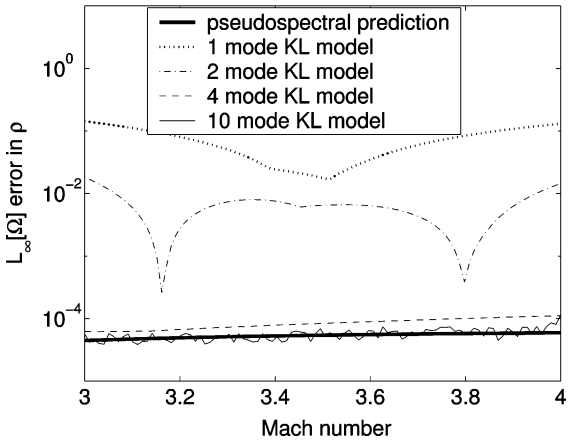

Fig. 7. KL model $L_\infty[\Omega]$ error in ρ for a 17×9 grid, $\mathscr{M}_\infty \in [3,4], b = 0.5$. A highly resolved 33×17 grid solution is the standard for the reported errors.

in $\rho(\xi,\eta)$ decreases with increasing number of KL modes until the approximate accuracy of the samples is reached around 5×10^{-5}. Once the accuracy of the snapshots has been reached, there is no further improvement in the accuracy with increasing number of KL modes, since the higher-order modes do not contain relevant information; they are corrupted by numerical error in the KL modes. For finer grid solutions than the 22×12 grid, the KL model accuracy became very sensitive to the ω_I^q in Eq. (57); therefore, the 22×12 grid KL model is the finest grid KL model employed in the current work.

7. Single variable design problem

To illustrate the use of a KL model for an optimal design problem, the power law body described parametrically in Eqs. (30) and (31) is considered, and the value of b is sought which minimizes the drag coefficient, C_D for fixed freestream Mach number, $\mathscr{M}_\infty = 3.5$, and ratio of specific heats, $\gamma = 7/5$. For the axisymmetric problem, the equation for $C_D(b)$ is

$$C_{\mathrm{D}}(b) = \frac{4}{\gamma \mathscr{M}_\infty^2} \int_0^1 pr \left.\frac{\partial r}{\partial \xi}\right|_{\eta=0} \mathrm{d}\xi. \tag{58}$$

The integral in Eq. (58) is evaluated by using Gauss quadrature to achieve high accuracy in C_{D} comparable to the accuracy in p and r from Eq. (58).

7.1. Error convergence for 10 snapshot KL model, $b \in [1/3,1/2]$, $\mathscr{M}_\infty = 3.5$

Before finding the value of b which minimizes C_{D} from Eq. (58), a KL model is built with 10 uniformly spaced snapshots that span the design space in which the minimum is expected, that is $b \in [1/3, 1/2]$ for $\mathscr{M}_\infty = 3.5$. Here, the snapshots are generated using the pseudospectral solver described in [2,4] on a 17×9 grid. A plot of the eigenvalues of density as a function of KL mode number is shown in Fig. 8, while the 10 normalized KL modes are shown in Fig. 9. There is a rapid decrease in the magnitude of the eigenvalues and the KL modes become topologically richer as the mode number increases. A convergence plot of the $L_\infty[\Omega]$ error in $\rho(\xi,\eta)$ with respect to the number of KL modes is shown in Fig. 10, where the error is measured against a highly resolved 33×17 grid solution of the pseudospectral solver. After the fourth mode there is no further improvement in the accuracy of the model, since the KL model accuracy has reached the level of error in the samples. Although the accuracy of the KL model is slightly better than the pseudospectral method when the ninth and tenth modes are included, this is fortuitous and is not expected in general, since the accuracy of the KL model should only be as accurate as the solution samples from which the modes were computed.

The distribution of $L_\infty[\Omega]$ error in $\rho(\xi,\eta)$ for the KL model over the entire range, $b \in [1/3, 1/2]$ is shown in Fig. 11. Once again, the $L_\infty[\Omega]$ error decreases with increasing number of KL modes until the approximate accuracy of the samples is reached around 5×10^{-5}. Once the accuracy of the snapshots has been reached, there is no further improvement in the accuracy with increasing number of KL modes, since the higher-order modes do not contain relevant information; they are corrupted by numerical error in the KL modes.

7.2. Minimum drag body shape

Since we are interested in the drag coefficient, C_{D}, in Fig. 12, we show the error convergence in C_{D} as a function of number of KL modes in the model over the range of geometric parameter $b \in [1/3, 1/2]$. The

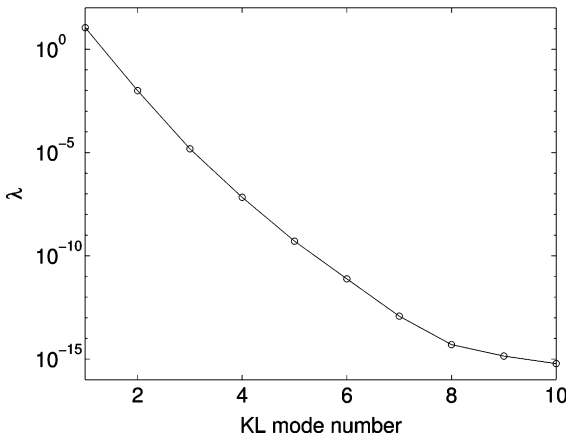

Fig. 8. Eigenvalues of density for 10 snapshots over the range $b \in [1/3, 1/2]$.

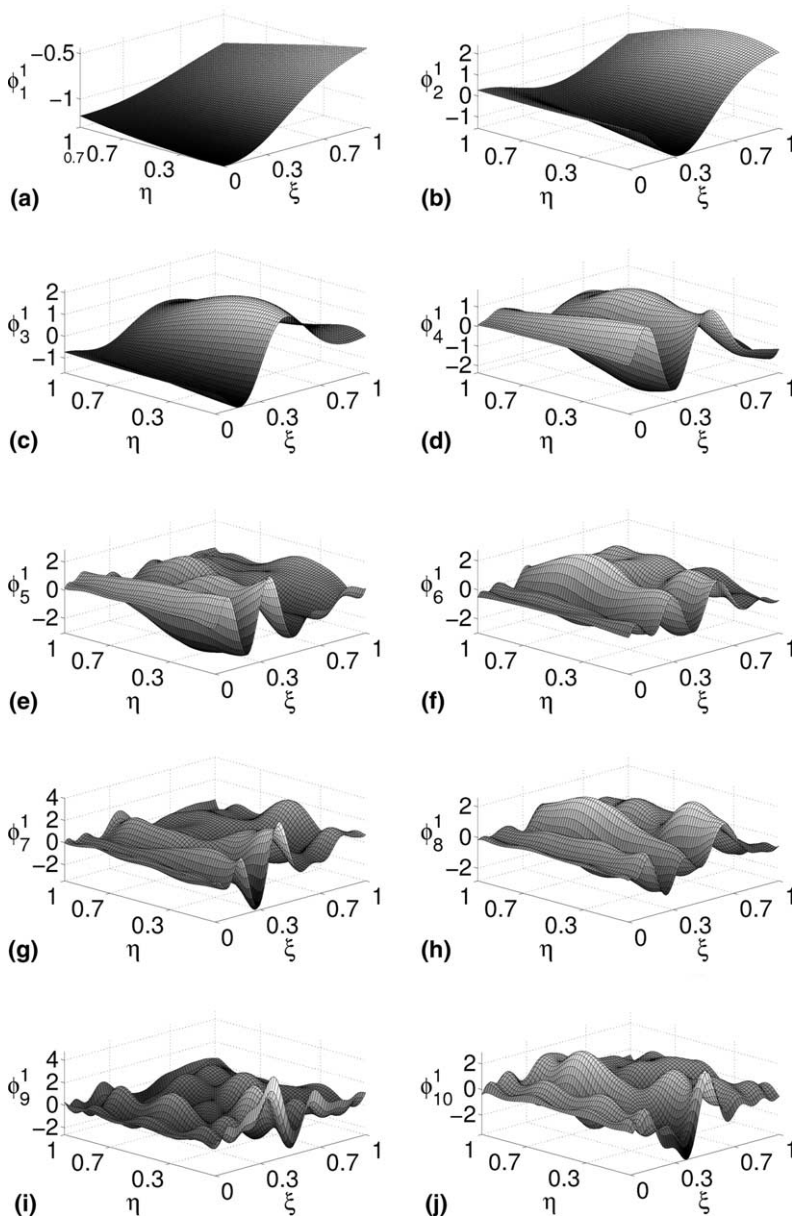

Fig. 9. Ten KL eigenmodes of density with associated eigenvalues, λ, generated from 10 snapshots in the range $b \in [1/3, 1/2]$. (a) $\lambda_1 = 11.1$, (b) $\lambda_2 = 9.9 \times 10^{-3}$, (c) $\lambda_3 = 1.5 \times 10^{-5}$, (d) $\lambda_4 = 6.8 \times 10^{-8}$, (e) $\lambda_5 = 5.1 \times 10^{-10}$, (f) $\lambda_6 = 7.6 \times 10^{-12}$, (g) $\lambda_7 = 1.2 \times 10^{-13}$, (h) $\lambda_8 = 5.0 \times 10^{-15}$, (i) $\lambda_9 = 1.4 \times 10^{-15}$ and (j) $\lambda_{10} = 6.0 \times 10^{-16}$.

KL model was built from 10 snapshots distributed uniformly over the range $b \in [1/3, 1/2]$; the snapshots were solved on a 17×9 grid. Again, the error is measured against a highly resolved 33×17 grid solution of the pseudospectral solver. It is seen that the error in the KL model is higher than the error in the pseudospectral solver over part of the range of b and lower over another part even with all 10 modes used in the KL model. It may be that there is fortuitous cancelling of errors in the integration to find C_D, which

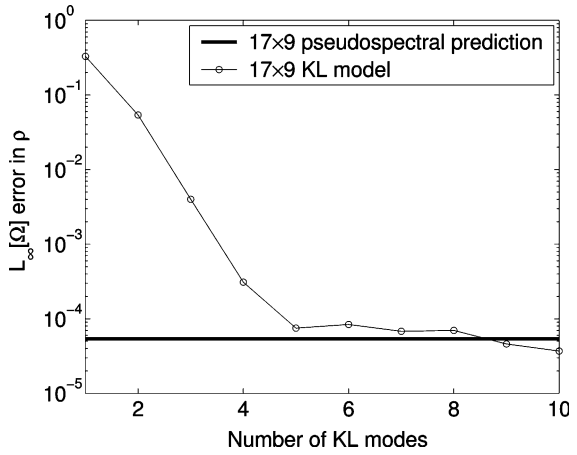

Fig. 10. KL model $L_\infty[\Omega]$ error in ρ for a 17×9 grid, $\mathscr{M}_\infty = 3.5, b = 0.5$. A highly resolved 33×17 grid solution is the standard for the reported errors.

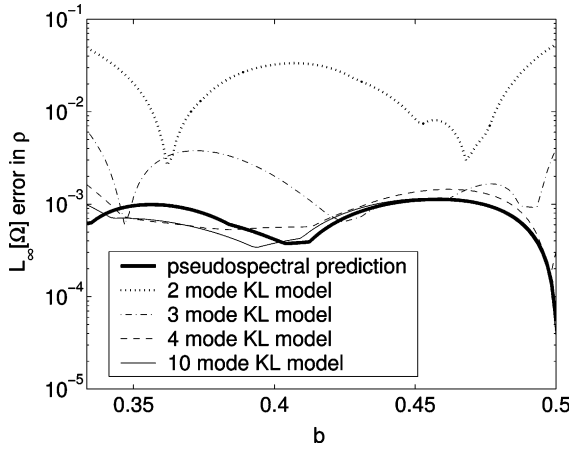

Fig. 11. KL model $L_\infty[\Omega]$ error in ρ for a 17×9 grid, $b \in [1/3, 1/2]$, $\mathscr{M}_\infty = 3.5$. A highly resolved 33×17 grid solution is the standard for the reported errors.

over part of the range of b favors the pseudospectral method and over another part favors the KL model. This is likely, since the plot of $L_\infty[\Omega]$ error in $\rho(\xi, \eta)$ from Fig. 11 shows convergence in number of KL modes to the level of accuracy in the snapshots.

In Figs. 13 and 14, we show the plot of C_D versus b for KL models using various numbers of KL modes compared to C_D from the pseudospectral solver on the same 17×9 grid. It is seen that for the KL model with one or two modes, the prediction is fairly poor; in fact, for the case of one KL mode, the trend of decreasing C_D with increasing b is the opposite of what it should be. Including at least three KL modes in the model yields very good agreement with the actual solution. There is a bias error in the prediction of C_D versus b for KL models with greater than four modes. The bias error is on the order of the error for the pseudospectral prediction on a 17×9 grid, Fig. 11, from which the KL model was developed, so that this bias error is within the error tolerance of the KL model.

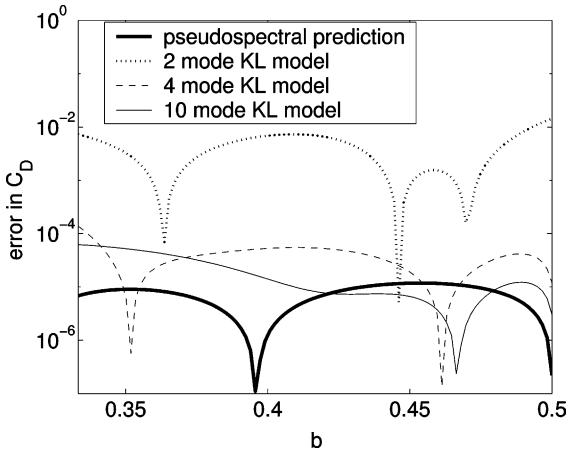

Fig. 12. KL model $L_\infty[\Omega]$ error in ρ for a 17×9 grid, $b \in [1/3, 1/2]$, $\mathscr{M}_\infty = 3.5$. A highly resolved 33×17 grid solution is the standard for the reported errors.

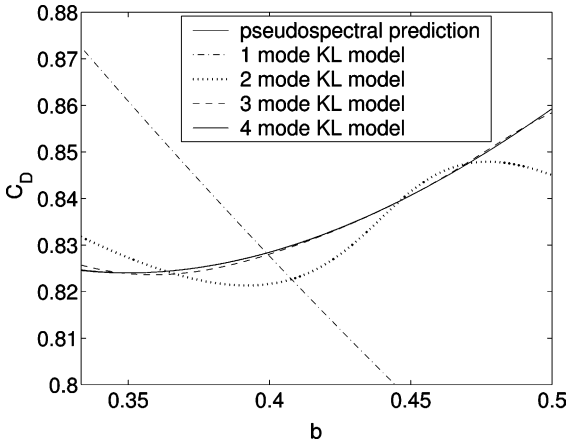

Fig. 13. C_D versus b for the KL model built from 10 snapshots on a 17×9 grid, $\mathscr{M}_\infty = 3.5$.

7.3. Efficiency of Karhunen–Loève model versus pseudospectral solver

To calculate efficiency, we plot the accuracy versus CPU time in seconds. For the pseudospectral solver, increasing solution accuracy is accomplished by refining the grid. For the KL model, there are two ways to increase accuracy: (1) increase the number of modes in the model and (2) use KL modes in the model which are taken from higher accuracy snapshots, i.e., refined grid solutions. It is evident from Fig. 6 that lower accuracy in the snapshots, 17×9 grid as compared to the 22×12 grid, does not appreciably affect the convergence rate until the baseline accuracy level is reached at 5×10^{-5}. Since the computational cost of the KL model is dependent on both the number of nodes in the snapshots through the Gauss quadrature formula as well as the number of modes, the KL model with the least computational cost for a given level of accuracy is achieved by employing snapshots with this desired level of accuracy, and also using only the minimum number of modes necessary to achieve the desired level of accuracy. That is, for greatest efficiency, build the KL model from snapshots with the fewest nodes and retain the fewest modes possible

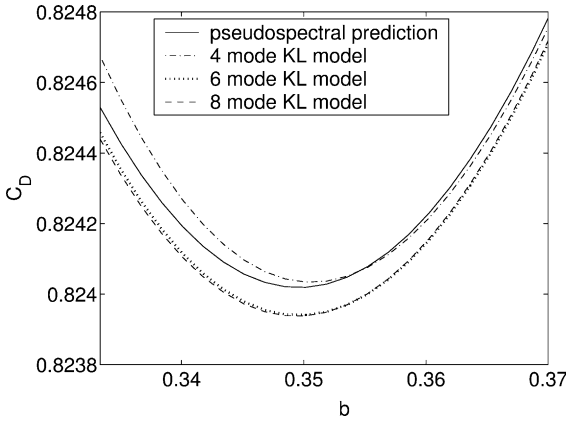

Fig. 14. Magnification of C_D versus b for the KL model built from 10 snapshots on a 17×9 grid, $\mathscr{M}_\infty = 3.5$.

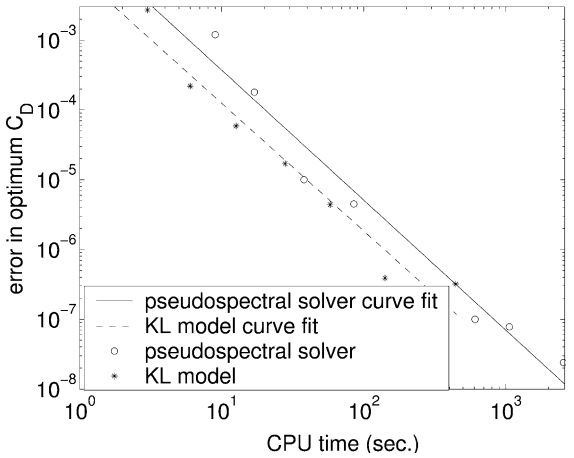

Fig. 15. Error in the optimum C_D versus CPU cost in seconds for the KL model and pseudospectral solver, $\mathscr{M}_\infty = 3.5$. A highly resolved 33×17 grid solution is the standard for the reported errors.

which will still achieve the desired level of accuracy. Fig. 15 shows the error in the optimum C_D versus CPU time in seconds for the KL model and pseudospectral method along with linear fits of the data points to make comparison easier. The data points representing the KL model are all from KL models built with 10 uniform snapshots over the range $b \in [1/3, 1/2]$ but with the levels of grid refinement and number of modes chosen for greatest efficiency, as just described. The various data points representing the pseudospectral solutions are found by varying the number of grid points; finer grids yield more accurate results but also take longer to compute. In Fig. 15 it is seen that the KL model and pseudospectral method predictions have the same slope of error versus CPU time with the KL model a factor of two less CPU time for the same level of accuracy. The calculations for both the pseudospectral solver and KL least-squares model were performed on a Pentium III, 500 MHz PC with 320 MB of RAM.

Further understanding of the efficiency of the KL least-squares method can be gained by examining the operation count required in the computational algorithm as compared to the pseudospectral method. For the two-dimensional problem considered here, the KL method requires $O(PLNM)$ operations, where P is the number of times Eq. (57) is called by the routine DUMINF, L is the number of modes in the KL model, and

N and M are the number of nodes in spatial direction ξ and η, respectively. The pseudospectral method requires $O(P'(N^2M + M^2N))$ operations, where P' is the number of time steps required to reach a steady-state solution. For the current problem, it was found that choosing $L \approx N/2$, $M \approx N/2$, and $P = P'$ yielded KL and pseudospectral solutions with the same level of accuracy, so that the operation count for both the pseudospectral and KL methods is $O(PN^3)$. This explains why the computational cost of the KL least-squares method is nearly identical to that of the pseudospectral method for the same level of accuracy as shown in Fig. 15.

8. Conclusions

In this study, a KL least-squares model of the Euler equations for supersonic flow over a blunt body was developed. It is believed that this is the first study where the KL method has been applied to a supersonic problem with shock-fitting. In addition, this work is novel in employing the KL method for a complex geometry with a physical boundary which is not known a priori.

The error convergence rate for the KL model is rapid, with the maximum accuracy level achieved with less than 10 KL modes for the single design variable problem posed. The maximum accuracy of the KL model is theoretically limited to the accuracy of the snapshots from which the model was built, and numerical results have been shown here which support this theoretical limit.

Due to the nature of the nonlinearity introduced into the problem through the grid metric terms, the integrals in the KL least-squares model are recomputed for every iteration of the DUMINF minimization routine; the result is a loss of efficiency such that the KL least-squares model is only slightly more efficient than the pseudospectral solver. This lack of a clear computational advantage of the KL method over the pseudospectral or other high accuracy numerical methods for certain nonlinear problems is something that has not received adequate attention in the literature to this point. Results of other researchers, Park and Jung [16], for example, which show a significant reduction in computational cost of the KL method over the pseudospectral method are performed on problems with fixed domains and simple nonlinearities. By fixing the physical domain of the problem, the grid metric terms in the governing equations are known a priori, and the nonlinearity of the problem becomes only quadratic for the incompressible Euler or Navier–Stokes equations. For sufficiently simple forms, it is possible to evaluate the integrals in the KL Galerkin model once at the time of building the model, rather than every time that the model needs to be evaluated.

The sampling required for the KL model construction raises other issues about how many samples to take and where in the design space to sample in order to guarantee a certain level of accuracy in the KL model without making the sampling procedure prohibitively expensive. Other high accuracy solvers which typically make use of polynomials or trigonometric basis functions do not require any sampling and may be preferred over the KL method for certain applications.

Although the topology of the current problem is simple enough to permit a single domain solution, for problems with slightly more complex geometries, multiple shocks, for example, a more general shock-fitting scheme such as that proposed by Nasuti and Onofri [39], coupled with a multi-domain pseudospectral method such as that proposed by Kopriva [40] is more useful. Although this work has shown promise in fitting complex two-dimensional shock structures, much work remains to be done, such as extending the method to three dimensions and to unstructured grids. Furthermore, for solutions with a large number of embedded discontinuities whose location is not known a priori, a multi-domain method with shock-fitting may become prohibitively complicated. Even if shock-fitting for problems with complex shock structures is possible, the additional difficulty of changes in the physical domain of the problem causing a significant loss in the efficiency of the KL model must be overcome. For these reasons, it is our opinion that the KL method is best suited to problems where the integrals can be evaluated a priori, restricting its use to problems with either fixed or simple moving boundaries. In addition, the computational cost incurred in the

sampling portion of constructing the KL model should receive serious consideration before deciding to employ the KL method for a specific application.

References

[1] P.A. Gnoffo, J.K. Weilmuenster, H.H. Hamilton, D.R. Olynick, E. Venkatapathy, Computational aerothermodynamic design issues for hypersonic vehicles, J. Spacecraft Rockets 36 (1) (1999) 21–43.

[2] G.P. Brooks, A Karhunen–Loève least-squares technique for optimization of geometry of a blunt body in supersonic flow, Ph.D. Dissertation, University of Notre Dame, Notre Dame, IN, 2003.

[3] G.P. Brooks, J.M. Powers, A Karhunen–Loève Galerkin technique with shock-fitting for optimization of a blunt body geometry, AIAA Paper 2002-3861, 2002.

[4] G.P. Brooks, J.M. Powers, A pseudospectral approximation of a blunt body in supersonic flow, J. Comput. Phys., 2003 (in review).

[5] D.A. Kopriva, T.A. Zang, M.Y. Hussaini, Spectral Methods for the Euler equations: the blunt body problem revisited, AIAA J. 29 (9) (1991) 1458–1462.

[6] D. Gottlieb, S. Orszag, Numerical Analysis of Spectral Methods: Theory and Applications, SIAM/CBMS, Philadelphia, 1977.

[7] J.F. Rodriguez, J.E. Renaud, B.A. Wujek, R.V. Tappeta, Trust region model management in multidisciplinary design optimization, J. Comput. Appl. Math. 124 (2000) 139–154.

[8] S.M. Batill, M.A. Stelmack, Framework for multidisciplinary design based on response-surface approximations, J. Aircraft 36 (1) (1999) 287–297.

[9] A. Jameson, Re-engineering the design process through computation, J. Aircraft 36 (1) (1999) 36–50.

[10] J. Reuther, J.J. Alonso, M.J. Rimlinger, A. Jameson, Aerodynamic shape optimization of supersonic aircraft configurations via an adjoint formulation on distributed memory parallel computers, Comput. Fluids 28 (1999) 675–700.

[11] J.J. Reuther, A. Jameson, J.J. Alonso, M.J. Rimlinger, D. Saunders, Constrained multipoint aerodynamic shape optimization using an adjoint formulation and parallel computers, Parts 1-2, J. Aircraft 36 (1) (1999) 51–74.

[12] J.L. Lion, Optimal Control of Systems Governed by Partial Differential Equations, Springer-Verlag, Berlin, 1971.

[13] H.M. Park, M.W. Lee, An efficient method of solving the Navier–Stokes equations for flow control, Int. J. Numer. Methods Engrg. 41 (1998) 1133–1151.

[14] A. Theodoropoulou, R.A. Adomaitis, E. Zafiriou, Model reduction for optimization of rapid thermal chemical deposition systems, IEEE Trans. Semicond. Manuf. 11 (1) (1998) 85–98.

[15] P.A. LeGresley, J.J. Alonso, Airfoil design optimization using reduced order models based on proper orthogonal decomposition, AIAA Paper 2000-2545, 2000.

[16] H.M. Park, W.S. Jung, Numerical solution of optimal magnetic suppression of natural convection in magneto-hydrodynamic flows by empirical reduction of modes, Comput. Fluids 31 (2002) 309–334.

[17] W.H. Jou, W.P. Huffman, D.P. Young, R.G. Melvin, M.B. Bieterman, C.L. Hilmes, F.T. Johnson, Practical considerations in aerodynamic design optimization, AIAA Paper 95-1730-CP, 1995.

[18] N. Aubry, P. Holmes, J.L. Lumley, E. Stone, The dynamics of coherent structures in the wall region of a turbulent boundary layer, J. Fluid Mech. 192 (1988) 115–173.

[19] L. Sirovich, H. Park, Turbulent thermal convection in a finite domain: Part I. Theory, Phys. Fluids A 2 (9) (1990) 1649–1658.

[20] H. Park, L. Sirovich, Turbulent thermal convection in a finite domain: Part II. Numerical results, Phys. Fluids A 2 (9) (1990) 1659–1668.

[21] C.-C. Chen, H.-C. Chang, Accelerated disturbance damping of an unknown distributed system by nonlinear feedback, AIChE J. 38 (9) (1992) 1461–1476.

[22] H.M. Park, D.H. Cho, The use of the Karhunen–Loève decomposition for the modeling of distributed parameter systems, Chem. Engrg. Sci. 51 (1) (1996) 81–98.

[23] H.M. Park, J.H. Lee, A method of solving inverse convection problems by means of mode reduction, Chem. Engrg. Sci. 53 (9) (1998) 1731–1744.

[24] H.M. Park, J.H. Lee, Reduction of modes for the solution of inverse natural convection problems, Comput. Methods Appl. Mech. Engrg. 190 (2000) 919–940.

[25] H.M. Park, J.H. Lee, Solution of an inverse heat transfer problem by means of empirical reduction of modes, Z. Ang. Math. Phys. 51 (2000) 17–38.

[26] H.M. Park, W.S. Jung, Recursive solution of an inverse heat transfer problem in rapid thermal processing systems, Int. J. Heat Mass Transfer 44 (2001) 2053–2065.

[27] H.M. Park, W.S. Jung, The Karhunen–Loève Galerkin method for the inverse natural convection problems, Int. J. Heat Mass Transfer 44 (2001) 155–167.

[28] H.M. Park, T.Y. Yoon, Solution of inverse radiation problems using the Karhunen–Loève Galerkin procedure, J. Quant. Spectrosc. Radiat. Transfer 68 (2001) 489–506.
[29] H.M. Park, M.W. Lee, An efficient method of solving the Navier–Stokes equations for flow control, Int. J. Numer. Methods Engrg. 41 (1998) 1133–1151.
[30] H.M. Park, M.W. Lee, Boundary control of the Navier–Stokes equation by empirical reduction of modes, Comput. Methods Appl. Mech. Engrg. 188 (2000) 165–186.
[31] H.M. Park, M.W. Lee, Control of Navier–Stokes equations by means of mode reduction, Int. J. Numer. Methods Fluids 33 (2000) 535–557.
[32] P.A. LeGresley, J.J. Alonso, Dynamic domain decomposition and error correction for reduced order models, AIAA Paper 2003-0250, 2003.
[33] D.J. Lucia, Reduced order modeling for high speed flows with moving shocks, Ph.D. Dissertation, Air Force Institute of Technology, Wright–Patterson Air Force Base, Ohio, 2001.
[34] K. Karhunen, Zur spektraltheorie stochastischer prozesse, Ann. Acad. Sci. Fen. 34 (1946).
[35] M. Loève, Probability Theory, Van Nostrand, Princeton, NJ, 1955.
[36] J. Lumley, Stochastic Tools in Turbulence, Academic Press, New York, 1970.
[37] A. Rosenfeld, A.C. Kak, Digital Picture Processing, Academic Press, New York, 1976.
[38] L. Sirovich, Turbulence and the dynamics of coherent structures. Parts 1–3, Quart. Appl. Math. 45 (3) (1987) 561–590.
[39] F. Nasuti, M. Onofri, Analysis of unsteady supersonic viscous flows by a shock-fitting technique, AIAA J. 34 (7) (1996) 1428–1434.
[40] D.A. Kopriva, Computation of hyperbolic equations on complicated domains with patched and overset Chebyshev grids, SIAM. J. Sci. Statist. Comput. 10 (1) (1989) 120–132.